BSLIM: Spectral Localization by Imaging With Explicit B_0 Field Inhomogeneity Compensation

Ildar Khalidov*, Dimitri Van De Ville, Mathews Jacob, François Lazeyras, and Michael Unser

***Abstract*—Magnetic resonance spectroscopy imaging (MRSI) is an attractive tool for medical imaging. However, its practical use is often limited by the intrinsic low spatial resolution and long acquisition time. Spectral localization by imaging (SLIM) has been proposed as a non-Fourier reconstruction algorithm that incorporates spatial *a priori* information about spectroscopically uniform compartments. Unfortunately, the influence of the magnetic field inhomogeneity—in particular, the susceptibility effects at tissues' boundaries—undermines the validity of the compartmental model. Therefore, we propose BSLIM as an extension of SLIM with field inhomogeneity compensation. A B_0-field inhomogeneity map, which can be acquired rapidly and at high resolution, is used by the new algorithm as additional *a priori* information. We show that the proposed method is distinct from the generalized SLIM (GSLIM) framework. Experimental results of a two-compartment phantom demonstrate the feasibility of the method and the importance of inhomogeneity compensation.**

***Index Terms*—Chemical shift imaging, constrained reconstruction, magnetic field inhomogeneity, magnetic resonance spectroscopy imaging (MRSI).**

I. Introduction

MAGNETIC resonance spectroscopy (MRS) has become an important tool in medical imaging; in particular, in human and animal neuroimaging [1], [2]. The measured magnetic resonance (MR) spectrum provides valuable information about metabolite concentrations; these can be estimated by fitting algorithms such as LCModel [3]. The volume of interest (VOI) is selected by dedicated radio-frequency (RF) pulse sequences, such as PRESS [4], [5] and STEAM [6] for ^{1}H MRS. However, the use of volume selection sequences has its shortcomings; most notably, restrictions on the shape of the VOI [7] and contamination of the spectrum by surrounding tissue [8]. Other solutions to localize the spectrum include the use of surface coils [9].

The combination of the spectroscopic information of MRS with the spatial resolution and localization of MR imaging (MRI) has a high potential for clinical applications. Magnetic resonance spectroscopic imaging (MRSI) consists in measuring the chemical shift at several k space positions [10]–[12]. Each k space position is selected by phase-encoding, followed by a long acquisition time to collect spectroscopic data. Clearly, maintaining a reasonable experiment duration makes the achievable resolution for MRSI much lower than for MRI; typically, 16×16 to 32×32 at 1.5 T. This low spatial resolution, combined with large metabolite concentration differences between adjacent tissues, exacerbates the artifacts of Fourier series reconstruction. In particular, the violation of the band-limited assumption introduces a so-called "voxel bleeding," which causes strong spectral contamination between neighboring voxels. Mathematically, the effect is characterized by a convolution with the spatial response function (SRF). Another important problem is the influence of the main field (B_0) inhomogeneity and the magnetic susceptibility effects near tissue boundaries; these result in a broadening and shifting effect on the spectral peaks. Carefully applied shimming techniques [13], [14] can substantially reduce the effect of the scanner's field inhomogeneity. However, the apparent local magnetic field is still altered by the susceptibility effects, which can significantly shift the spectrum on the ppm-scale. Difficulties with low spatial resolution and field inhomogeneity have limited the utility of MRSI for *in vivo* studies.

Many methods have been proposed to improve the performance of MRSI, either by increasing the reconstruction quality or by speeding up the acquisition time. These methods include: imposing a limited spatial support on the reconstruction to limit the effect of the SRF [15], [16]; optimizing k space trajectories [17]–[19]; adjusting the SRF using higher-order gradients [20]; sampling partial k space data [21]; and, applying sensitivity encoding (SENSE) [22].

Here, we focus on the "spectral localization by imaging" (SLIM) method [23], which is a non-Fourier reconstruction algorithm that aims at improving the effective resolution using *a priori* spatial information. The main idea fits within the paradigm of "parametric imaging" [24] and "constrained reconstruction" [25], [26]. The basic assumption is that the specimen is partitioned into compartments with spatially homogeneous spectra. The knowledge of the compartments is extracted from a standard high-resolution MR image. While SLIM might appear highly attractive, its practical use is limited by the homogeneity assumption within each compartment. Liang and Lauterbur identified (B_0) magnetic field distortions as the main source

Manuscript received October 20, 2006; revised February 16, 2007. This work was supported in part by the Center for Biomedical Imaging (CIBM) of the Geneva—Lausanne Universities in part by the EPFL, in part by the foundations Leenaards and Louis-Jeantet, and in part by the Swiss National Science Foundation under Grant 200020-109415. *Asterisk indicates corresponding author.*

*I. Khalidov is with the Biomedical Imaging Group, EPFL, CH-1015 Lausanne, Switzerland (e-mail: ildar.khalidov@epfl.ch).

D. Van De Ville and M. Unser are with the Biomedical Imaging Group, EPFL, CH-1015 Lausanne, Switzerland (e-mail: dimitri.vandeville@epfl.ch; michael.unser@epfl.ch).

M. Jacob is with the Department of Biomedical Engineering, University of Rochester Medical Center, Rochester, NY 14642 USA (e-mail: mathews.jacob@rochester.edu).

F. Lazeyras is with the Department of Radiology, University Hospital of Geneva, CH-1211 Geneva 1 (e-mail: francois.lazeyras@sim.hcuge.ch).

Color versions of one or more of the figures in this paper are available online at http://ieeexplore.ieee.org.

Digital Object Identifier 10.1109/TMI.2007.897385

of inhomogeneity inside a compartment, and they proposed generalized SLIM (GSLIM) as an extended framework to deal with SLIM's shortcomings [27]. The solution that GSLIM provides to the field inhomogeneity problem is indirect. The model allows for spatial variations and these are estimated from the data; the ill-posedness of the problem is dealt with by using regularization techniques.

In this paper, we propose BSLIM: an extension to the original SLIM method that includes a suitable compensation for the magnetic field inhomogeneity. In addition to the high-resolution MR image that is required to extract the compartmental information, the method relies on the measurement (after shimming) of the field inhomogeneity map (e.g., by using the AUTOSHIM technique [13]). Such a map includes both the scanner field inhomogeneity and the object-dependent magnetic susceptibility effects. The *a priori* information is fed into our extended BSLIM signal model, which then allows to find the compartments' spectra as the solution of a least-squares problem.[1] By taking advantage of the block-diagonal structure of the formulation, we obtain an algorithm that is as fast as the original SLIM method. An important point is that our model is distinct from the one used in GSLIM. The proposed reconstruction algorithm is a direct approach that exploits the additional information of the field inhomogeneity map, without increasing of the number of parameters to estimate. The feasibility of the method is illustrated on synthetic and experimental data.

II. BSLIM Approach

A. Theory

Let $\mathbf{x}$ be the spatial domain variable and f the temporal frequency. We describe the magnetic field by its strength perpendicular to the slice that is measured as $B_0 + \Delta B_0(\mathbf{x})$, where $\Delta B_0(\mathbf{x})$ is the spatially varying component that accounts for the total inhomogeneity; i.e., the local field variations due to scanner imperfections and object-dependent susceptibility effects. The object being imaged is characterized by the so-called "spectral function" $\rho(\mathbf{x}, f)$, which represents the spatial distribution of the spectral information. The free induction decay signal of this object during a phase-encoding spectroscopic experiment, acquired in the presence of a field with inhomogeneity map $\Delta B_0(\mathbf{x})$, can then be mathematically expressed as

$$s(\mathbf{k}_i, t) = \int_{-\infty}^{\infty} \int_{\mathcal{D}_\mathbf{x}} \rho(\mathbf{x}, f) e^{-j2\pi\gamma\Delta B_0(\mathbf{x})t - j2\pi(\mathbf{k}_i\cdot\mathbf{x}+ft)} \mathrm{d}\mathbf{x}\mathrm{d}f \quad (1)$$

$$= \int_{-\infty}^{\infty} \int_{\mathcal{D}_\mathbf{x}} \rho\left(\mathbf{x}, f - \Delta f(\mathbf{x})\right) e^{-j2\pi(\mathbf{k}_i\cdot\mathbf{x}+ft)} \mathrm{d}\mathbf{x}\mathrm{d}f \quad (2)$$

where $\mathcal{D}_\mathbf{x}$ is the field-of-view (FOV) and where $\mathbf{k}_i$, $i = 1, \ldots, M$, indicate the k space locations. In the last equation, we introduced the local spectral shift as $\Delta f(\mathbf{x}) = \gamma \Delta B_0(\mathbf{x})$, where γ is the gyromagnetic ratio, which shows that the measurements are equivalent to those obtained from an object with modified density $\rho(\mathbf{x}, f - \Delta f(\mathbf{x}))$ in the presence of an homogeneous magnetic field.

As in the case of SLIM, we assume that the spectral function can be described by K spectroscopically uniform compartments, each of them designated by an indicator function

$$\chi_k(\mathbf{x}) = \begin{cases} 1, & \mathbf{x} \in \text{compartment } k \\ 0, & \text{otherwise} \end{cases}$$

and their spectra $q_k(f)$, $k = 1, \ldots, K$. The standard spectral function $\rho_{\mathrm{SLIM}}(\mathbf{x}, f)$ then takes the form

$$\rho_{\mathrm{SLIM}}(\mathbf{x}, f) = \sum_{k=1}^{K} q_k(f)\chi_k(\mathbf{x}). \quad (3)$$

The measurement model of (1) and (2) suggests how to include the effect of the field inhomogeneity in the spectral function. Specifically, we propose the modified function

$$\rho_{\mathrm{BSLIM}}(\mathbf{x}, f) = \rho_{\mathrm{SLIM}}\left(\mathbf{x}, f - \Delta f(\mathbf{x})\right) = \sum_{k=1}^{K} q_k\left(f - \Delta f(\mathbf{x})\right)\chi_k(\mathbf{x}) \quad (4)$$

which can be used as if the magnetic field were homogeneous; i.e., BSLIM compensates for the presence the inhomogeneity map. Assuming the BSLIM model, the expected measurements is rewritten as

$$\begin{aligned} s_{\mathrm{BSLIM}}(\mathbf{k}_i, t) &= \int_{-\infty}^{\infty} \int_{\mathcal{D}_\mathbf{x}} \sum_{k=1}^{K} \chi_k(\mathbf{x}) q_k\left(f - \Delta f(\mathbf{x})\right) \\ &\quad \times e^{-j2\pi(\mathbf{k}_i\cdot\mathbf{x}+ft)} \mathrm{d}\mathbf{x}\mathrm{d}f \\ &= \sum_{k=1}^{K} \int_{-\infty}^{\infty} \int_{\mathcal{D}_\mathbf{x}} \chi_k(\mathbf{x}) q_k(f) \\ &\quad \times e^{-j2\pi\Delta f(\mathbf{x})t - j2\pi(\mathbf{k}_i\cdot\mathbf{x}+ft)} \mathrm{d}\mathbf{x}\mathrm{d}f \quad (5) \\ &= \sum_{k=1}^{K} Q_k(t) \int_{\mathcal{D}_\mathbf{x}} \chi_k(\mathbf{x}) \\ &\quad \times e^{-j2\pi\Delta f(\mathbf{x})t - j2\pi\mathbf{k}_i\cdot\mathbf{x}} \mathrm{d}\mathbf{x} \quad (6) \end{aligned}$$

where $Q_k(t) = \int_{-\infty}^{\infty} q_k(f) e^{-j2\pi ft} \mathrm{d}f$. Introducing the BSLIM kernels

$$H_k(\mathbf{k}_i, t) = \int_{\mathcal{D}_\mathbf{x}} \chi_k(\mathbf{x}) e^{-j2\pi\Delta f(\mathbf{x})t - j2\pi(\mathbf{k}_i\cdot\mathbf{x})} \mathrm{d}\mathbf{x} \quad (7)$$

we finally obtain a linear system of equations

$$s_{\mathrm{BSLIM}}(\mathbf{k}_i, t) = \sum_{k=1}^{K} Q_k(t) H_k(\mathbf{k}_i, t) \quad (8)$$

where $Q_k(t)$ are the unknown free induction decay (FID) functions and where the $H_k(\mathbf{k}_i, t)$ include all the *a priori* knowledge.

[1] A preliminary version of this work was presented at MedIm 2006 [28]. During the first review cycle of the present manuscript, a paper that describes a similar approach appeared in press [29]. There, the low-resolution voxels are considered as compartments and regularization is used to make the inverse problem well-posed.

Note that we have been able to essentially decouple the effect of the distortions by expressing the measurement equation in the time domain [cf. (6)]; this constitutes the main originality of our approach.

The problem can now be stated as a least-squares (LS) minimization: given the measurements $s(\mathbf{k}_i, t)$, the compartments $\chi_k(\mathbf{x})$, and the inhomogeneity map $\Delta f(\mathbf{x})$, find the BSLIM FIDs $Q_k(t)$ that best fit the measurements. This can be expressed as

$$\{Q_k(t)\}_{k=1,\ldots,K} = \arg\min_{\{Q_k(t)\}} \int_{\mathcal{D}_t} \sum_{i=1}^{M} \left| s(\mathbf{k}_i, t) - \sum_{k=1}^{K} Q_k(t) H_k(\mathbf{k}_i, t) \right|^2 \mathrm{d}t \quad (9)$$

where $\mathcal{D}_t$ indicates the acquisition window in the temporal domain. For the case $\Delta f(\mathbf{x}) = 0$, we recover the standard SLIM method where the kernel is time-independent; i.e., $H_k(\mathbf{k}_i, t) = H_k(\mathbf{k}_i)$. So the BSLIM extension changes the 2-D kernels into 3-D ones. Fortunately, the minimization problem of (9) can still be solved for each time-point independently; i.e., for a specific t_0, we can find $Q_k(t_0)$ such that

$$\{Q_k(t_0)\}_{k=1,\ldots,K} = \arg\min_{\{Q_k(t_0)\}} \sum_{i=1}^{M} \left| s(\mathbf{k}_i, t_0) - \sum_{k=1}^{K} Q_k(t_0) H_k(\mathbf{k}_i, t_0) \right|^2. \quad (10)$$

B. Comparison With GSLIM

GSLIM proposes a generalized series extension of the classical SLIM model. The main idea is to express the model as

$$\rho_{\mathrm{GSLIM}}(\mathbf{x}, f) = \sum_{n=1}^{M} a_n(f) \varphi_n(\mathbf{x}, f) \quad (11)$$

where $a_n(f)$ are the generalized spectra to be estimated and where $\varphi_n(\mathbf{x}, f)$ are basis functions. The choice of the basis functions proposed in [27] is

$$\varphi_n(\mathbf{x}, f) = \rho_{\mathrm{SLIM}}(\mathbf{x}, f) e^{j2\pi \mathbf{k}_n \cdot \mathbf{x}} \quad (12)$$

which leads to the GSLIM spectral function

$$\rho_{\mathrm{GSLIM}}(\mathbf{x}, f) = \sum_{n=1}^{M} \sum_{k=1}^{K} a_n(f) q_k(f) \chi_k(\mathbf{x}) e^{j2\pi \mathbf{k}_n \cdot \mathbf{x}}. \quad (13)$$

The spectra $q_k(f)$, which are part of the basis functions, are estimated beforehand using standard SLIM. Under the model of (13), the expected measurements become

$$s_{\mathrm{GSLIM}}(\mathbf{k}_i, t) = \sum_{n=1}^{M} \sum_{k=1}^{K} \int_{-\infty}^{\infty} a_n(f) q_k(f) e^{-j2\pi f t} \mathrm{d}f \times \int_{\mathcal{D}_\mathbf{x}} \chi_k(\mathbf{x}) e^{-j2\pi(\mathbf{k}_i - \mathbf{k}_n)\cdot \mathbf{x}} \mathrm{d}\mathbf{x}.$$

TABLE I
OVERVIEW OF THE VARIOUS SAMPLING GRIDS INVOLVED IN THE COMPUTATIONAL ALGORITHM

Sampling grid	Description	Typical range
$\{\mathbf{x}_n\}_{n=1,\ldots,N}$	High-resolution spatial domain	$N = 256 \cdot 256$
$\{\mathbf{k}_i\}_{i=1,\ldots,M}$	Low-resolution k-space	$M = 16 \cdot 16$
$\{f_l\}_{l=1,\ldots,L}$	Limited-support spectral domain	$L = 64$
$\{t_m\}_{m=1,\ldots,T}$	Temporal domain	$T = 1024$

In order to obtain a linear system of equations, one transforms the measurements in the temporal Fourier domain

$$\mathcal{F}_t\{s_{\mathrm{GSLIM}}\}(\mathbf{k}_i, f) = \sum_{n=1}^{M} a_n(f) \sum_{k=1}^{K} q_k(f) \int_{\mathcal{D}_\mathbf{x}} \chi_k(\mathbf{x}) e^{-j2\pi(\mathbf{k}_i - \mathbf{k}_n)\cdot \mathbf{x}} \mathrm{d}\mathbf{x} \quad (14)$$

$$= \sum_{n=1}^{M} a_n(f) G(\mathbf{k}_i - \mathbf{k}_n, f) \quad (15)$$

where we recognize the GSLIM kernel

$$G(\mathbf{k}, f) = \sum_{k=1}^{K} q_k(f) \int_{\mathcal{D}_\mathbf{x}} \chi_k(\mathbf{x}) e^{-j2\pi \mathbf{k}\cdot\mathbf{x}} \mathrm{d}\mathbf{x}. \quad (16)$$

A close comparison between (6) and (15) shows that BSLIM cannot be cast into the GSLIM framework: the parameters $a_n(f)$ to be estimated are linked to the k space positions and not to the compartments, while the kernel acts as a multiplication in the spectral domain instead of a multiplication in the temporal domain. Nevertheless, it should be noted that an alternative choice of the basis functions would allow to generalize BSLIM in a similar way

$$\varphi_n(\mathbf{x}, f) = \rho_{\mathrm{BSLIM}}(\mathbf{x}, f) e^{j2\pi \mathbf{k}_n \cdot \mathbf{x}}. \quad (17)$$

C. Computational Algorithm

For a practical algorithm, we need to deal with the various sampling grids involved. We denote the discretized versions of the continuous-domain functions by the same symbol, but with the arguments between square brackets. An overview of the various grids that are used is given in Table I.

The input data to the core algorithm is represented as follows:

- $\chi_k[\mathbf{x}_n]$: the K indicator functions of the compartments on a high-resolution grid in the spatial domain;
- $\Delta f[\mathbf{x}_n]$: the spectral shift due to the field inhomogeneity map $\Delta B_0[\mathbf{x}_n]$;
- $s[\mathbf{k}_i, t_m]$: the MRSI measurements on the low-resolution k space grid.

The first important step of the algorithm is to precompute the kernels $H_k[\mathbf{k}_i, t_m]$. For that purpose, let us first consider the kernel of (7) in the spatio-spectral domain

$$h_k(\mathbf{x}, f) = \mathcal{F}_x \left\{ \mathcal{F}_t^{-1}\{H_k\} \right\} \quad (18)$$

$$= \chi_k(\mathbf{x}) \delta\left(f - \Delta f(\mathbf{x})\right) \quad (19)$$

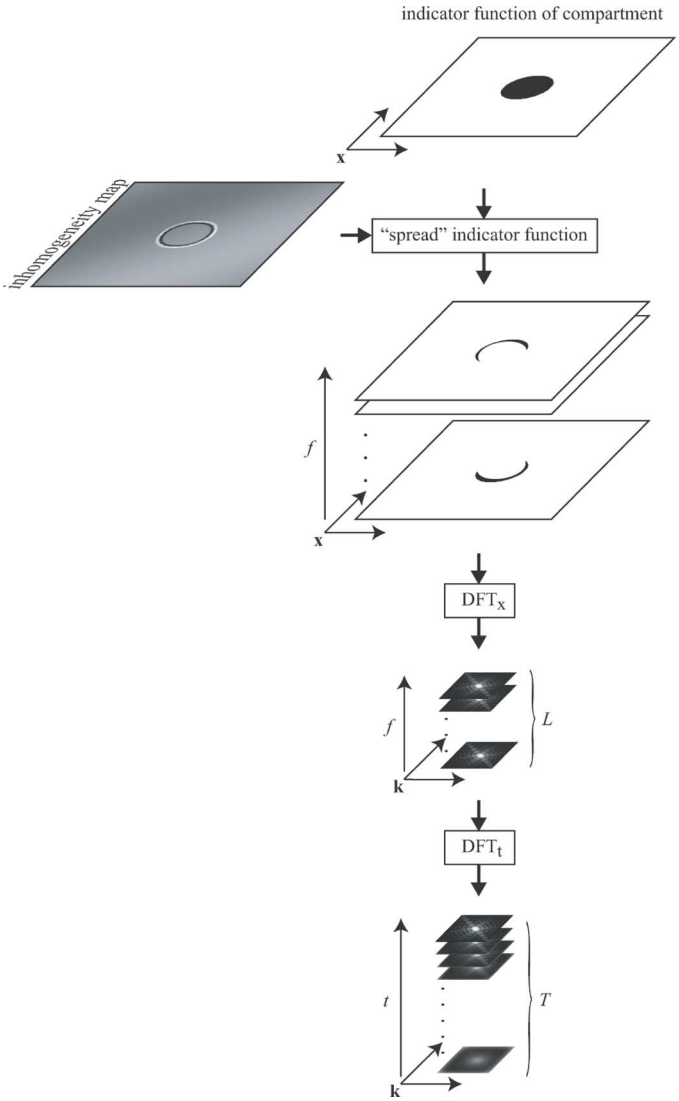

Fig. 1. Schematic overview of the computation of the BSLIM kernels $H_k[\mathbf{k}_i, t_m]$.

where δ represents the Dirac distribution. We now propose a discretized version of h_k that is obtained by spectrally redistributing the indicator function as follows:

$$h_k[\mathbf{x}_n, f_l] = \begin{cases} \chi_k[\mathbf{x}_n], & f_l \text{ closest to } \Delta f[\mathbf{x}_n] \\ 0, & \text{otherwise} \end{cases}. \tag{20}$$

The sampling grid $\{f_l\}$ is chosen at the spectral resolution that corresponds to the temporal sampling frequency of the measured data, but the length of its support L is limited to the width of the range for $\Delta f[\mathbf{x}_n]$. Next, the spatial-domain discrete Fourier transform (DFT) is applied to obtain the low-resolution k space samples $\mathrm{DFT}_x\{h_k\}[\mathbf{k}_i, f_l]$. Finally, the temporal-domain inverse DFT is applied after zero padding of the spectral samples, up to length T, to obtain the BSLIM kernels

$$H_k[\mathbf{k}_i, t_m] = \mathrm{DFT}_t^{-1}\left\{\mathrm{DFT}_x\{h_k\}\right\}. \tag{21}$$

In Fig. 1, we show a schematic overview of the computation of the kernels.

The solution of the LS fitting problem

$$Q_k[t_m] = \arg\min_{Q_k[t_m]} \sum_i \left| s[\mathbf{k}_i, t_m] - \sum_{k=1}^{K} H_k[\mathbf{k}_i, t_m] Q_k[t_m] \right|^2 \tag{22}$$

is then formulated using the matrices

$$\mathbf{H}[t_m] = \begin{bmatrix} H_1[\mathbf{k}_1, t_m] & H_2[\mathbf{k}_1, t_m] & \dots & H_K[\mathbf{k}_1, t_m] \\ H_1[\mathbf{k}_2, t_m] & H_2[\mathbf{k}_2, t_m] & \dots & H_K[\mathbf{k}_2, t_m] \\ & & \ddots & \\ H_1[\mathbf{k}_M, t_m] & H_2[\mathbf{k}_M, t_m] & \dots & H_K[\mathbf{k}_M, t_m] \end{bmatrix} \tag{23}$$

$$\mathbf{Q}[t_m] = \begin{bmatrix} Q_1[t_m] \\ Q_2[t_m] \\ \vdots \\ Q_K[t_m] \end{bmatrix}, \quad \mathbf{s}[t_m] = \begin{bmatrix} s[\mathbf{k}_1, t_m] \\ s[\mathbf{k}_2, t_m] \\ \vdots \\ s[\mathbf{k}_M, t_m] \end{bmatrix} \tag{24}$$

as

$$\mathbf{Q}[t_m] = \left(\mathbf{H}^*[t_m]\mathbf{H}[t_m]\right)^{-1} \mathbf{H}^*[t_m]\mathbf{s}[t_m]. \tag{25}$$

The computation of $\mathbf{Q}[t_m]$ boils down to one $K \times K$ matrix inversion per time-point, which is of the same complexity as the standard SLIM algorithm.

D. Overview of the Proposed Method

The complete procedure of our approach consists of the following steps:

1) Acquisition:
   a) shimming;
   b) prescan;
      i) high-resolution field inhomogeneity map;
      ii) high-resolution proton density image;
   c) MRSI scan using phase encoding.
2) BSLIM algorithm:
   a) segmentation to obtain the compartmental information;
   b) precomputation of kernels;
   c) LS fit.

The BSLIM algorithm was implemented using MATLAB 7 of The Mathworks Inc.

III. Materials and Methods

A. Synthetic Data

We first demonstrate the feasibility of our method using synthetic data. The dataset is generated for a simulated phantom whose configuration is shown in Fig. 2(a). The FOV is a square $[-0.5 \dots 0.5] \times [-0.5 \dots 0.5]$. The compartments are characterized by two ellipses (see Table II), which are reconstructed from their analytical Fourier transform [30, App.1] on a standard Cartesian sampling grid $\{\mathbf{x}_n\}$ of size 256 × 256 (i.e., $N = 256^2$).

Each of the three compartments has a single spectral component, as shown in Fig. 2(b); the number of samples in the temporal dimension is fixed at $T = 1024$. The inhomogeneity map is also reconstructed from its analytical Fourier domain

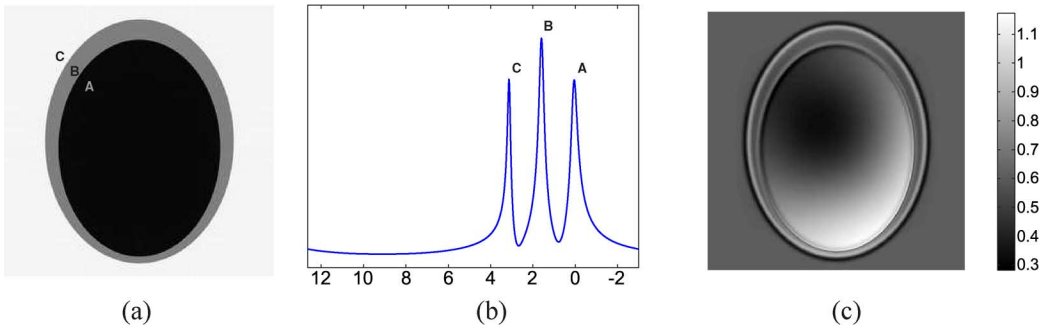

Fig. 2. (a) Configuration of the simulated phantom. (b) Spectral components of each compartment. (c) Hypothetical inhomogeneity map.

TABLE II
PARAMETERS OF THE SIMULATED PHANTOM

Ellipse	Horizontal semiaxis	Vertical semiaxis	x_0	y_0
Outer	0.35	0.45	0	0
Inner	0.3	0.4	0	-0.025

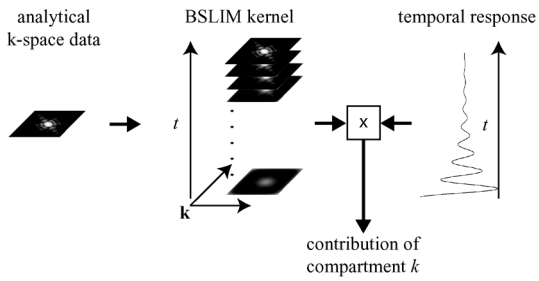

Fig. 3. The kth compartment is modeled analytically in the k space. Its contribution to the synthetic data is computed by reconstruction on a high-resolution grid and multiplication with the temporal response of the metabolite.

expression, which is taken as a laplacian-of-Gaussian-filtered reference image (the full width at half maximum of the Gaussian filter is 5 pixel units). This simulates the effect of changes in magnetic susceptibility between the compartments, see Fig. 2(c). A smooth "pincushion" component is added to model the scanner-dependent field imperfections. The dynamic range of the inhomogeneity map is chosen such that the maximal spectral shift corresponds to 1 ppm. The synthetic data is obtained from the precise high-resolution images and the B_0 map: the corresponding kernels $H_k[\mathbf{k}_i, t_m]$ are determined and multiplied by the oscillating decaying exponential of the spectral component in each compartment, see Fig. 3. Note that the compartment images that are used at the synthesis step are high-resolution reconstructions from the analytical Fourier-domain model. This simulates the measurement process for an ideal object. BSLIM, on the contrary, uses indicator (binary) compartment images, obtained by segmentation. Also, BSLIM quantizes the B_0 map, which our synthesis method does not do. Thus, BSLIM reconstruction will not match the original spectra exactly.

To illustrate the effect of the number of phase-encoding steps, we simulate two datasets with different resolutions; i.e., a 5×1 and 8×8 Cartesian sampling grid in k space. Finally, an experiment is carried out where we add white Gaussian noise ($\mathrm{SNR} = 18.5\,\mathrm{dB}$) to the simulated MRSI measurements. Time-domain windowing is performed on the resulting FIDs for all methods.

B. Two-Compartment Phantom Data

We acquired a dataset using a physical two-compartment phantom. The inner compartment (sphere of diameter 8.7 cm) contained a solution of 50 mmol/L (mM) N-acetyl-aspartate (NAA) and 50 mM of creatine (Cr) in doped water. A spectral reference marker (0 ppm) was used, consisting of 3 mM of 3-(trimethylsilyl)-1-propanesulfonic acid (DSS). The outer compartment (cylinder of height 13.5 cm and of diameter 10.5 cm) was filled with corn oil. The scanner was a Philips Gyroscan 1.5 T. We selected a 10-mm slice in the middle of the phantom with $\mathrm{FOV} = 160 \times 160$ mm and applied first-order shimming to compensate at best the field inhomogeneity. Next, the remaining field variations were measured using the AUTOSHIM two-step procedure [13]. This method is fast (only two high-resolution MRI acquisitions are needed); with our scanner, it added 90 s to the total acquisition time. Importantly, it measures all field distortions, including those caused by variations of magnetic susceptibility. The TE parameter is chosen in a way such that the water and the fat peaks are superimposed (due to carefully tuned aliasing). The phase difference between the two MR images is used to extract the local field inhomogeneity, see Fig. 4(b). Also, a high-resolution proton density image was acquired to obtain the configuration of the phantom, as shown in Fig. 4(a). The high-resolution grid was again the standard Cartesian sampling grid of size 256×256. Finally, the phase-encoded water-suppressed MRSI dataset on a 16×16 k space sampling grid was acquired, using 1024 time-points for each k space location ($\mathrm{TR} = 1600$ ms, $\mathrm{TE} = 288$ ms, bandwidth $= 1$ kHz). We visualized the dataset using Fourier reconstruction on a 16×16 Cartesian grid in Fig. 4(c). In this experiment, no volume selection nor spatial saturation slabs were applied. To evaluate the results, we also measured the spectrum inside each compartment using a PRESS pulse sequence for a 8 mm^3 volume selection. Since the compartments are relatively large, the PRESS spectra have a low degree of contamination.

The compartmental information was extracted from the proton density image using the standard watershed-based algorithm available in Matlab. We selected the two compartments corresponding to the outer and inner part of the phantom. The reconstruction was performed using two methods—BSLIM and

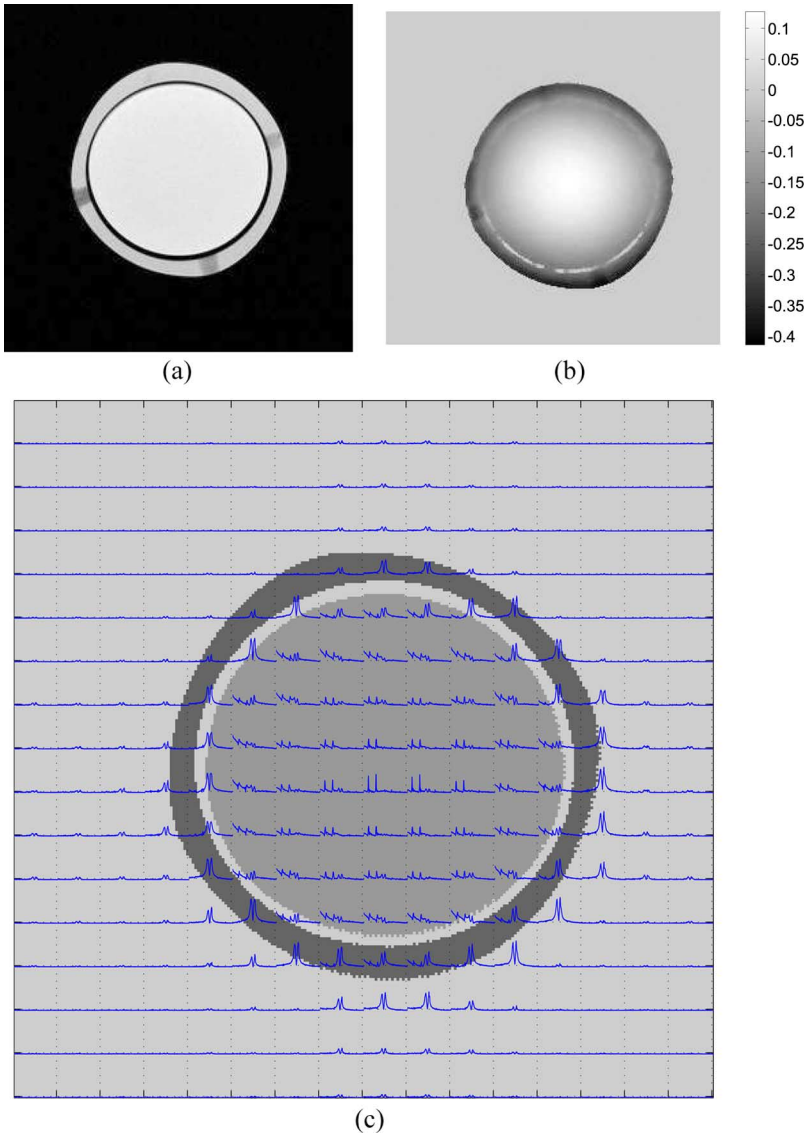

Fig. 4. Measured data for the two-compartment phantom. (a) Proton density image. (b) Inhomogeneity map. (c) The 16 × 16 spectra overlaid on the proton density image; the spatial-domain data was obtained using Fourier reconstruction.

noncompensated SLIM. Additional denoising (time-domain windowing) was performed on the resulting spectra.

IV. Results and Discussion

A. Synthetic Data

The compartmental spectra for the simulated MRSI data was reconstructed using the following techniques:

1) **Fourier reconstruction**: the k space data is zero-padded up to 256 × 256, and a spectrum is picked from the middle of each compartment;
2) **Standard SLIM**: which uses *a priori* knowledge about the compartments;
3) **BSLIM**: which further incorporates a field inhomogeneity compensation mechanism.

In Figs. 5 and 6, we show the true and reconstructed spectra for 5 × 1 and 8 × 8 phase-encoding steps, respectively.

We observe the incapacity of both Fourier and SLIM methods to recover the correct spectra, especially in compartment B. With the 5 × 1 measurements, the reconstructed spectra exhibit erroneous, "leaking" peaks that are even stronger than the true one. In the 8 × 8 case, the spurious peaks A and C still reach 50% of the height of the peak B. This kind of behavior is expected for the Fourier method which does not correct for the leakage at all. The SLIM approach, on the other hand, does account for the SRF effect, and its failure is only due to the nonhomogeneity of the field. In compartment A, the leakage is less pronounced but still important, especially for the 5 × 1 case. In compartment C, the contamination is not as strong as in the two others due to its larger size. Interestingly, with SLIM, the amplitudes of the resulting peaks are lower than expected. This is due to the fact that the SLIM model is not able to adequately fit the data. There is also a considerable frequency shift and peak broadening in the SLIM reconstruction induced by the inhomogeneity. The BSLIM method performs best for the given imaging model: the peaks are located at their exact places, and their shape matches that of the original ones.

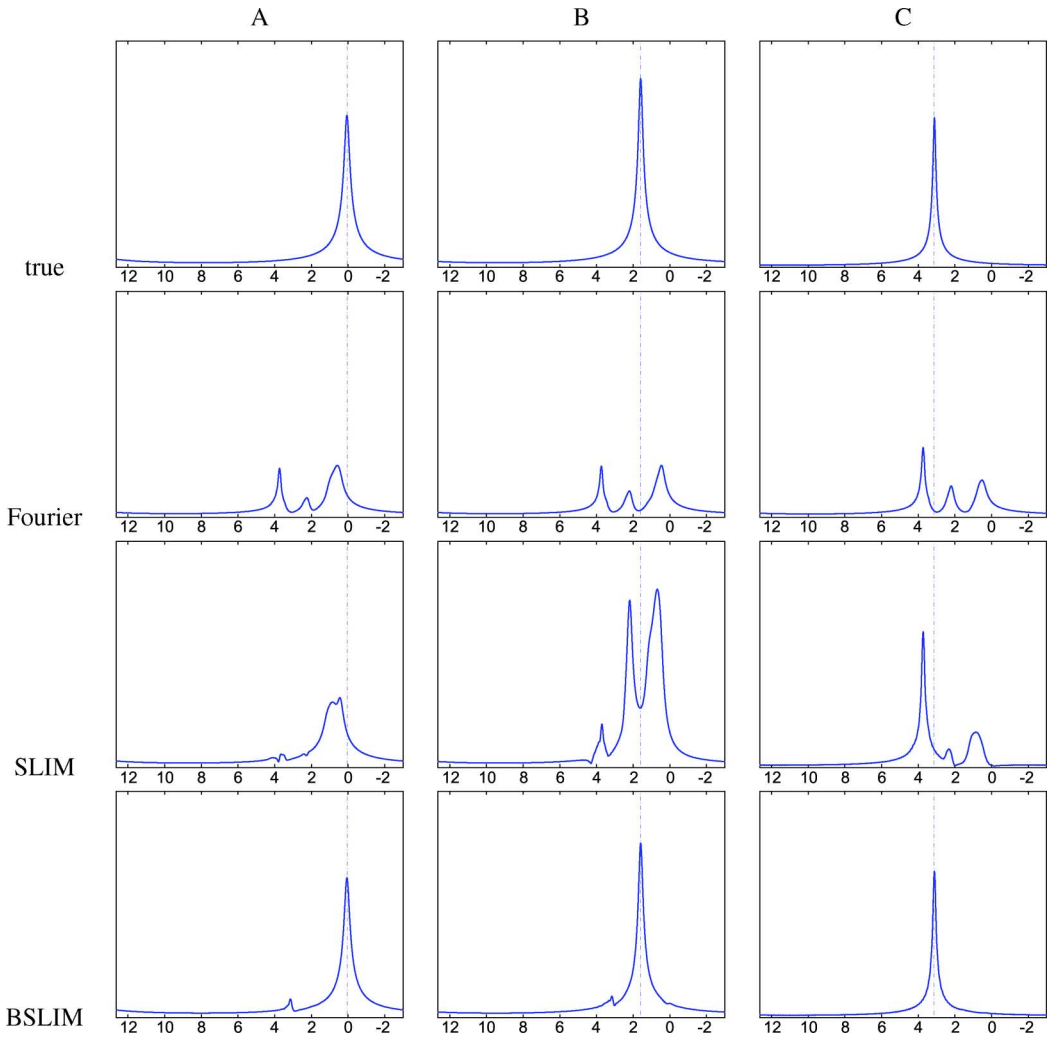

Fig. 5. True and reconstructed compartmental spectra from the simulated MRSI data with 5×1 phase-encoding steps. The Fourier reconstruction uses zero-padding to interpolate the missing data. SLIM and BSLIM both used the correct compartmental information, while BSLIM further compensated for the field inhomogeneity.

The reconstruction from the simulated noisy measurements is shown in Fig. 7. In general, additive noise is not an issue for SLIM-like methods, as they perform implicit averaging over the compartment. Comparing Figs. 6 and 7, we observe that the overall shape of the peaks is preserved for all methods. In Table III, we show the signal-to-noise ratio (SNR) of the reconstructed spectra in the case of noisy and noiseless measurements. We see that BSLIM loses 2 dB in the presence of additive noise. For the other two methods, the systematic error is so strong that it essentially masks the influence of noise.

Reconstruction using BSLIM takes a few seconds only; i.e., on an Apple Mac G5 (Dual 1.8 GHz, 1 GB RAM), the precomputation of the kernels took 8 s, and the LS fitting 0.5 s.

B. Two-Compartment Phantom Data

In Fig. 8, we show the reconstructed and reference spectra for the two compartments of the phantom. The ppm scale was chosen in such a way that the NAA peak is located at 2.02 ppm.

The results of BSLIM for the phantom experiment are shown in Figs. 8 and 9. We present the obtained spectra for the two compartments, showing also a magnified version of the spectral regions of interest. To understand the important improvements that we get when compared to the standard SLIM method, we show the spectrum for compartment 2 with the one obtained without inhomogeneity compensation. In Fig. 9, we observe that the spurious peak in the standard SLIM case is as high as the metabolite peak. Our algorithm outputs spectra in which the lipid peak is completely suppressed. In addition, by comparing the absolute intensity of the peaks in Fig. 9, we observe the strong improvement in the sensitivity of the algorithm to the metabolite signal. This could be explained by the loss of energy due to propagation of the spectra in the standard SLIM case.

C. Discussion

Our experiments confirm the fact that B_0 field inhomogeneity is an important obstacle to proper spectrum reconstruction. While the scanner-dependent inhomogeneity may eventually be avoided by using higher order shimming techniques, the object-dependent field variations are inevitable.

The SLIM method does not compensate for the B_0 field inhomogeneity, which causes broadening, shifting and leakage of the peaks. For metabolites having strong signal, the leakage is particularly noticeable. On the other hand, as seen in the two-compartment phantom case, the weaker signals generated

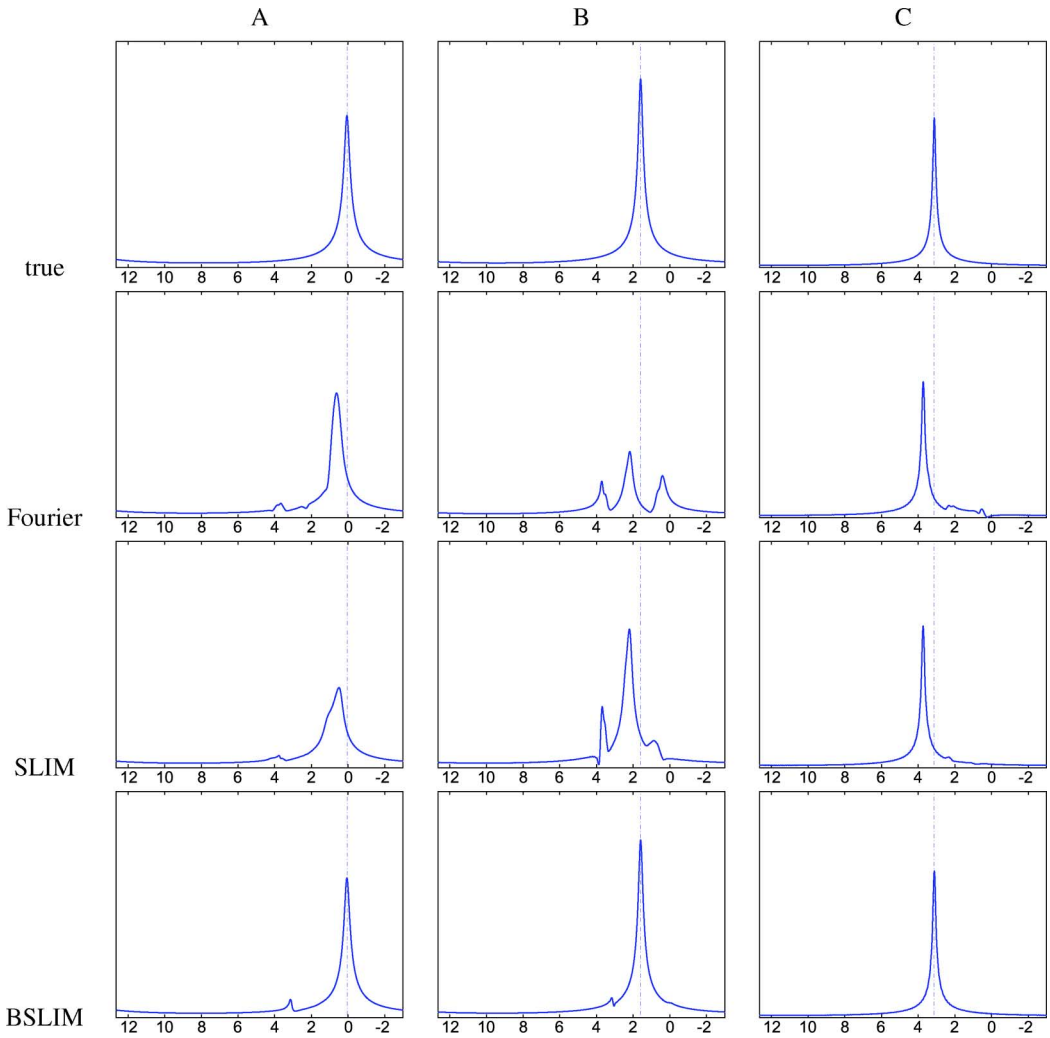

Fig. 6. True and reconstructed compartmental spectra from the simulated MRSI data with 8 × 8 phase-encoding steps. The Fourier reconstruction uses zero-padding to interpolate the missing data. SLIM and BSLIM both used the correct compartmental information, while BSLIM also took advantage of the known inhomogeneity map.

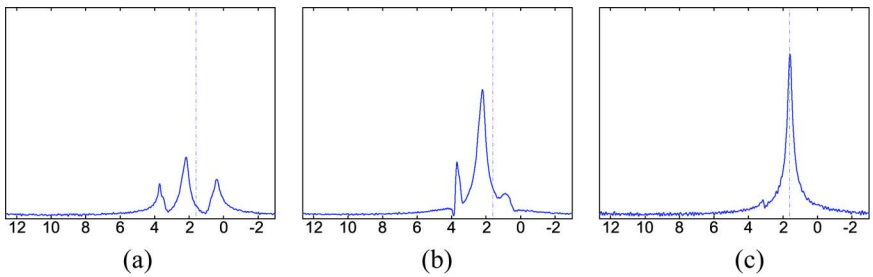

Fig. 7. Experiment results for simulated noisy MRSI data with 8 × 8 phase-encoding steps: reconstructed spectrum for compartment B. (a) Fourier reconstruction. (b) SLIM. (c) BSLIM.

by metabolites like NAA and Cr get diffused; in the SLIM-resolved spectra, the corresponding peaks become almost undistinguishable from noise. The performance of SLIM improves if one increases the spatial resolution of MRSI data. However, the need for longer acquisition times makes this approach inapplicable in practice.

The spectra obtained with BSLIM do not exhibit the mentioned artifacts. The results on synthetic data show that BSLIM can potentially work at low resolutions. The improvements do not come at the price of computational complexity; the latter remains the same as for SLIM. Importantly, the B_0 field measurement can be performed when the object is in the scanner, which allows BSLIM compensation for object-dependent field inhomogeneity.

The NL-CSI method of Yablonskiy *et al.* [29] is based on the same equation (6). However, the authors suggest a different experimental problem setting (1-D CSI voxel sequence, a significant number of compartments each corresponding to a voxel), which leads to a different approach that involves regularization. In our case, we take the full advantage of the high-resolution

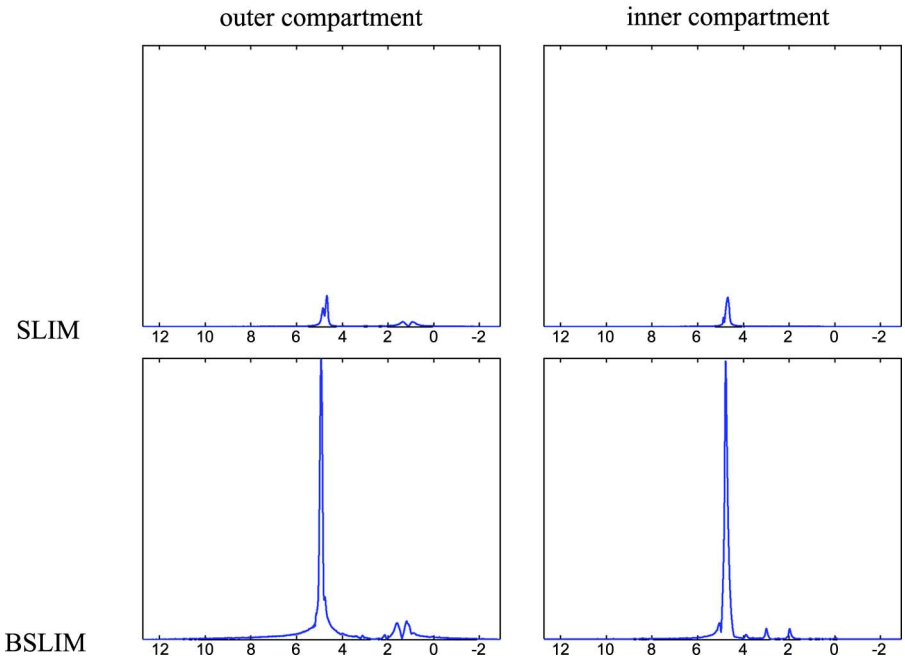

Fig. 8. Reconstructed compartmental spectra for the phantom.

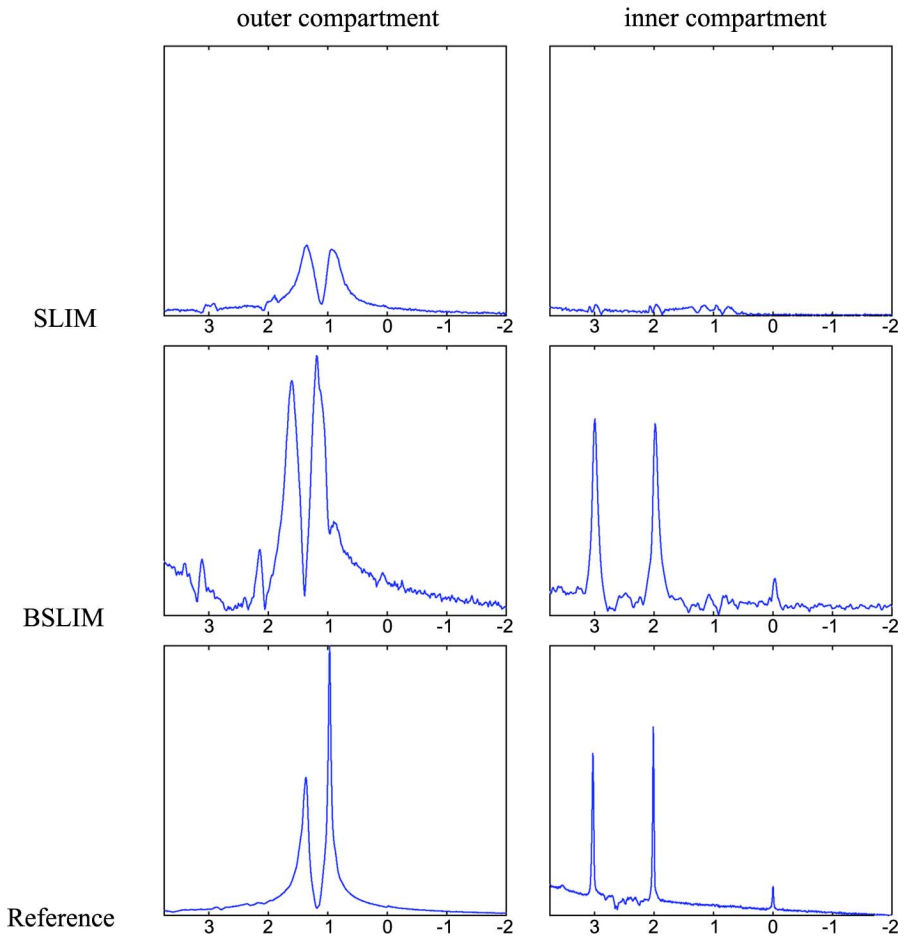

Fig. 9. Magnifications of the reconstructed and reference spectra (obtained using PRESS) for the phantom.

anatomical image and keep the number of compartments low, which results in a computationally efficient algorithm.

The uniform-compartment model is clearly an idealization, and it remains the most important limitation of the constrained imaging techniques such as (B)SLIM. In this respect, three important questions arise: 1) what is the performance of BSLIM when the compartments are not strictly homogeneous; 2) what is the performance of BSLIM if the compartments were not deter-

TABLE III
SNR OF THE RECONSTRUCTED SPECTRA FOR COMPARTMENT B (dB)

Method	Fourier	SLIM	BSLIM
Noiseless measurements	-0.22	-1.67	23.82
Noisy measurements (SNR=18.5 dB)	-0.22	-1.67	21.75

mined exactly; 3) whether or not it is possible to extend BSLIM to allow for spectral variations in the compartments.

The measurement model in BSLIM is an improved version of the SLIM one. After using BSLIM to compensate for B_0 field variations, we are still left with the compartmental inhomogeneity which is of anatomical nature. In this case, previous analyses done for SLIM are still valid [31], [32]. The important conclusion of these works is that SLIM is able to recover the average compartmental spectra for moderate intracompartment variations of 20% already when the number of phase-encoded signals is slightly more than the number of compartments. Since BSLIM only has to deal with residual inhomogeneities, its behaviour is expected to improve compared to what has been predicted in this area before.

The use of high-resolution compartment images makes the algorithm dependent on the segmentation procedure and on the precision with which the boundaries of the compartments are determined. Suppose that, after segmentation, the image for compartment A contains some parts that actually belong to compartment B. Once again, if the number of measurements is sufficient, Hu *et al.* have shown that the algorithm will recover the average spectrum quite adequately. In this case, the presence of the "wrong" signal B in the resolved spectrum will be approximately proportional to the area of compartment B that has been assigned to compartment A.

A possible extension of the BSLIM method for nonspectroscopically uniform compartments is suggested by GSLIM and (17); for instance, it may be possible to add degrees-of-freedom under the form of Fourier components at the k space sampling locations in order to adapt the shape of the indicator functions to the data. This generalization of BSLIM might also improve its robustness against segmentation imprecisions.

Another option may be to use an extended set of spatial basis functions χ_k; e.g., those varying linearly in space on the support of the compartment. Indeed, the problem model (9) allows possible integration of additional *a priori* knowledge derived from T1, T2, or PD-weighted images. The important point in our method is that it is a parametric, model-based approach. It is only as good as the underlying model is, and it will only work appropriately as long as there are more measurements than free parameters.

The BSLIM algorithm requires two additional MRI acquisitions compared to SLIM. With the scanner used for the experiments, the time that it takes to obtain the B_0 inhomogeneity map (90 s) would be sufficient to acquire 60 additional phase-encoded measurements, extending the grid from 16×16 to only 18×18. Therefore, we can state that the overhead of BSLIM is negligible compared to the MRSI acquisition times.

With the advantages mentioned, BSLIM has potential for applications that have successfully deployed SLIM or GSLIM before; e.g., in cardiac imaging [33], brain imaging [34]–[36], and drug monitoring [37]. The promising results on the 5×1 measurement grid suggest the possible use of BSLIM in fast, spatially localized metabolite tracking applications.

V. CONCLUSION

We have proposed a new algorithm (BSLIM) that solves the inverse problem in MRSI. Based on the ideas of SLIM, our method uses the MRI image of the object under investigation. At the same time, it also takes into account the *a priori* information on the B_0 field inhomogeneity. The results show significant improvement over the noncompensated SLIM technique in terms of spurious peak suppression, visual quality, and detectability of the metabolites. In terms of computational speed, the algorithm that we propose is quite comparable with the MRSI-version of SLIM.

The compensation capabilities and increased sensitivity of BSLIM might open a possibility of use of MRSI in challenging applications such as *in vivo* investigations.

REFERENCES

[1] B. Gimi, A. P. Pathak, E. Ackerstaff, K. Glunde, D. Artemov, and Z. M. Bhujwalla, "Molecular imaging of cancer: Applications of magnetic resonance methods," *Proc. IEEE*, vol. 93, no. 4, pp. 784–799, Apr. 2005.

[2] E. T. Ahrens, P. T. Narasimhan, T. Nakada, and R. E. Jacobs, "Small animal neuroimaging using magnetic resonance microscopy," *Prog. Nucl. Magn. Reson. Spectrosc.*, vol. 40, no. 4, pp. 275–306, Jun. 2002.

[3] S. W. Provencher, "Estimation of metabolite concentrations from localized in vivo proton NMR spectra," *Magn. Reson. Med.*, vol. 30, pp. 672–679, 1993.

[4] R. J. Ordidge, M. R. Bendall, R. E. Gordon, and A. Connelly, "Volume detection for in vivo spectroscopy," in *Magnetic Resonance in Biology and Medicine*. New Delhi, India: Tata-McGraw Hill, 1985, pp. 387–397.

[5] P. Bottomley, "Spatial localisation in NMR spectroscopy in vivo," *Ann. NY Acad. Sci.*, vol. 508, pp. 333–348, 1987.

[6] J. Frahm, K.-D. Merboldt, and W. Hänicke, "Localized proton spectroscopy using stimulated echoes," *J. Magn. Reson.*, vol. 72, pp. 502–508, 1987.

[7] T. Ernst, J. Hennig, D. Ott, and H. Friedburg, "The importance of the voxel size in clinical ^1H spectroscopy of the human brain," *NMR Biomed.*, vol. 2, pp. 216–224, 1989.

[8] S. F. Keevil and M. C. Newbold, "The performance of volume selection sequences for in vivo NMR spectroscopy: Implications for quantitative MRS," *Magn. Reson. Imag.*, vol. 19, no. 9, pp. 1217–1226, Nov. 2001.

[9] S. Nelson, D. Vigneron, J. Star-Lack, and J. Kurhanewicz, "High spatial resolution and speed in MRSI," *NMR Biomed.*, vol. 10, no. 8, pp. 411–422, 1997.

[10] T. R. Brown, B. M. Kincaid, and K. Ugurbil, "NMR chemical shift imaging in three dimensions," *Proc. Nat. Acad. Sci.*, vol. 79, pp. 3523–3526, 1982.

[11] A. A. Maudsley, S. K. Hilal, W. H. Perman, and H. E. Simon, "Spatially resolved high resolution spectroscopy by 'four-dimensional' NMR," *J. Magn. Reson.*, vol. 51, pp. 147–152, 1983.

[12] P. C. Lauterbur, D. N. Levin, and R. B. Marr, "Theory and simulation of NMR spectroscopic imaging and field plotting by projection reconstruction involving an intrinsic frequency dimension," *J. Magn. Reson.*, vol. 59, pp. 536–541, 1983.

[13] E. Schneider and G. Glover, "Rapid *in vivo* proton shimming," *Magn. Res. Med.*, vol. 18, pp. 335–347, Apr. 1991.

[14] R. Gruetter, "Automatic, localized in vivo adjustment of all first- and second-order shim coils," *Magn. Res. Med.*, vol. 29, no. 6, pp. 804–811, 1993.

[15] S. K. Plevritis and A. Macovski, "Spectral extrapolation of spatially bounded images," *IEEE Trans. Med. Imag.*, vol. 14, no. 3, pp. 487–497, Sep. 1995.

[16] J. Tsao, "Extension of finite-support extrapolation using the generalized series model for MR spectroscopic imaging," *IEEE Trans. Med. Imag.*, vol. 20, no. 11, pp. 1178–1182, Nov. 2001.

[17] S. Sarkar, K. Heberlein, and X. P. Hu, "Truncation artifact reduction in spectroscopic imaging using a dual-density spiral k-space trajectory," *Magn. Reson. Imag.*, vol. 20, no. 10, pp. 743–757, Dec. 2002.

[18] C.-M. Tsai and D. Nishimura, "Reduced aliasing artifacts using variable-density k-space sampling trajectories," *Magn. Res. Med.*, vol. 43, no. 3, pp. 452–458, 2000.

[19] Y. Gao and S. J. Reeves, "Optimal k-space sampling in MRSI for images with a limited region of support," *IEEE Trans. Med. Imag.*, vol. 19, no. 12, pp. 1168–1178, Dec. 2000.

[20] R. Pohmann, E. Rommel, and M. von Kienlin, "Beyond k-space: Spectral localization using higher order gradients," *J. Magn. Reson.*, vol. 141, no. 2, pp. 197–206, Dec. 1999.

[21] L. Yao, Y. Cao, and D. Levin, "2D locally focused MRI: Applications to dynamic and spectroscopic imaging," *Magn. Res. Med.*, vol. 36, no. 6, pp. 834–846, 1996.

[22] U. Dydak, M. Weiger, K. P. Pruessmann, D. Meier, and P. Boesiger, "Sensitivity-encoded spectroscopic imaging," *Magn. Reson. Med.*, vol. 46, pp. 713–722, 2001.

[23] X. Hu, D. Levin, P. Lauterbur, and T. Spraggins, "SLIM: Spectral localization by imaging," *Magn. Res. Med.*, vol. 8, pp. 314–322, 1988.

[24] E. Haacke, Z.-P. Liang, and S. Izen, "Constrained reconstruction: A superresolution, optimal signal-to-noise alternative to the Fourier transform in magnetic resonance imaging," *Med. Phys.*, vol. 16, no. 3, pp. 388–397, 1989.

[25] Z. P. Liang and P. C. Lauterbur, "Constrained imaging," *IEEE Eng. Med. Biol. Mag.*, vol. 15, no. 5, pp. 126–132, Sep. 1996.

[26] K. A. Wear, K. J. Myers, S. S. Rajan, and L. W. Grossman, "Constrained reconstruction applied to 2-D chemical shift imaging," *IEEE Trans. Med. Imag.*, vol. 16, no. 5, pp. 591–597, Oct. 1997.

[27] Z.-P. Liang and P. C. Lauterbur, "A generalized series approach to MR spectroscopic imaging," *IEEE Trans. Med. Imag.*, vol. 10, no. 2, pp. 132–137, Jun. 1991.

[28] I. Khalidov, D. Van De Ville, M. Jacob, F. Lazeyras, and M. Unser, "Improved MRSI with field inhomogeneity compensation," in *Proc. SPIE Int. Symp. Med. Imag.: Image Process. (MI'06)*, J. Reinhardt and J. Pluim, Eds., San Diego, CA, Feb. 11–16, 2006, vol. 6144, pp. 614 467-1–614 467-7.

[29] A. Bashir and D. Yablonskiy, "Natural linewidth chemical shift imaging (NL-CSI)," *Magn. Res. Med.*, vol. 56, no. 1, pp. 7–18, Jul. 2006.

[30] R. Van de Walle, H. Barrett, K. Myers, M. Altbach, B. Desplanques, A. Gmitro, J. Cornelis, and I. Lemahieu, "Reconstruction of MR images from data acquired on a general nonregular grid by pseudoinverse calculation," *IEEE Trans. Med. Imag.*, vol. 19, no. 12, pp. 1160–1167, Dec. 2000.

[31] X. Hu and Z. Wu, "SLIM revisited," *IEEE Trans. Med. Imag.*, vol. 12, no. 3, pp. 583–587, Sep. 1993.

[32] Z. P. Liang and P. C. Lauterbur, "A theoretical-analysis of the SLIM technique," *J. Magn. Reson. Ser. B*, vol. 102, no. 1, pp. 54–60, Aug. 1993.

[33] R. Loffler, R. Sauter, H. Kolem, A. Haase, and M. von Kienlin, "Localized spectroscopy from anatomically matched compartments: Improved sensitivity and localization for cardiac p-31 mrs in humans," *J. Magn. Reson.* , vol. 134, no. 2, pp. 287–299, Oct. 1998.

[34] G. D. Graham, A. M. Blamire, D. L. Rothman, L. M. Brass, P. B. Fayad, O. A. C. Petroff, and J. W. Prichard, "Early temporal variation of cerebral metabolites after human stroke—A proton magnetic-resonance spectroscopy study," *Stroke*, vol. 24, no. 12, pp. 1891–1896, Dec. 1993.

[35] B. A. Berkowitz, N. Bansal, and C. A. Wilson, "Noninvasive measurement of steady-state vitreous lactate concentration," *NMR Biomed.*, vol. 7, no. 6, pp. 263–268, Sep. 1994.

[36] J. A. Kmiecik, C. D. Gregory, Z. P. Liang, P. C. Lauterbur, and M. J. Dawson, "Lactate quantitation in a gerbil brain stroke model by GSLIM of multiple-quantum-filtered signals," *J. Magn. Reson. Imag.*, vol. 9, no. 4, pp. 539–543, Apr. 1999.

[37] J. R. Griffiths and J. D. Glickson, "Monitoring pharmacokinetics of anticancer drugs: Non-invasive investigation using magnetic resonance spectroscopy," *Adv. Drug Delivery Rev.*, vol. 41, no. 1, pp. 75–89, Mar. 2000.